

Unveiling defect-mediated carrier dynamics in monolayer semiconductors by spatiotemporal microwave imaging

Zhaodong Chu^{a,1}, Chun-Yuan Wang^{a,1}, Jiamin Quan^{a,1}, Chenhui Zhang^b, Chao Lei^a, Ali Han^b, Xuejian Ma^a, Hao-Ling Tang^b, Dishan Abeysinghe^a, Matthew Staab^a, Xixiang Zhang^b, Allan H. MacDonald^a, Vincent Tung^b, Xiaoqin Li^a, Chih-Kang Shih^a, and Keji Lai^{a,2}

^aDepartment of Physics, The University of Texas at Austin, Austin, TX 78712; and ^bPhysical Sciences and Engineering Division, King Abdullah University of Science and Technology, 23955-6900 Thuwal, Kingdom of Saudi Arabia

Edited by Todd D. Krauss, University of Rochester, Rochester, NY, and accepted by Editorial Board Member Richard Eisenberg April 30, 2020 (received for review March 5, 2020)

The optoelectronic properties of atomically thin transition-metal dichalcogenides are strongly correlated with the presence of defects in the materials, which are not necessarily detrimental for certain applications. For instance, defects can lead to an enhanced photoconduction, a complicated process involving charge generation and recombination in the time domain and carrier transport in the spatial domain. Here, we report the simultaneous spatial and temporal photoconductivity imaging in two types of WS2 monolayers by laser-illuminated microwave impedance microscopy. The diffusion length and carrier lifetime were directly extracted from the spatial profile and temporal relaxation of microwave signals, respectively. Time-resolved experiments indicate that the critical process for photoexcited carriers is the escape of holes from trap states, which prolongs the apparent lifetime of mobile electrons in the conduction band. As a result, counterintuitively, the long-lived photoconductivity signal is higher in chemical-vapor deposited (CVD) samples than exfoliated monolayers due to the presence of traps that inhibits recombination. Our work reveals the intrinsic time and length scales of electrical response to photoexcitation in van der Waals materials, which is essential for their applications in optoelectronic devices.

transition-metal dichalcogenides | defects | charge carriers | spatiotemporal dynamics | laser-illuminated microwave impedance microscopy

S emiconducting transition-metal dichalcogenides (TMDs) MX_2 (M = Mo, W; X = S, Se) exhibit remarkable electrical and optical properties (1-5), such as strong light-matter interaction in the infrared/visible range (6), good carrier mobility (7), and high photoresponsivity (8, 9). As in any materials, however, imperfections like structural defects are inevitable in TMD monolayers (10). Depending on the targeted application, the effect of impurities can be either detrimental or beneficial. For electronic devices, crystalline disorders are usually unwanted because of the adverse effect on carrier mobility (11, 12). For optoelectronic devices, however, the situation is more complicated. Certain defects are favorable for processes like single-photon emitting (13–16), which are important in quantum-emitters applications. Similar considerations also apply for photovoltaics (17) and photodetectors (18, 19), where the dynamics of photogenerated carriers play a key role. Photoconduction is a complex process involving the generation and recombination of electrons and holes, as well as the carrier diffusion from the illumination spot and transport under the electric field. While defects usually suppress carrier mobility, they may also elongate the lifetime of photocarriers. Their impact on the intrinsic photoconductivity is thus nontrivial. It is imperative to systematically investigate the spatiotemporal evolution of photoexcited carriers in various TMD monolayers with different levels of defects.

The conventional method to spatially resolve photoconduction is scanning photocurrent microscopy (SPCM) (20-23), which measures the transport across electrical contacts as a focused laser beam scans over the sample. The temporal response of this technique is limited by the carrier transit between electrodes and charge transfer at the metal-semiconductor junction, rather than the intrinsic photoresponse time of the material. The spatial resolution of SPCM is also diffraction-limited. In this work, we report the spatiotemporal study of photoexcited carriers in two types of WS₂ monolayers by laser-illuminated microwave impedance microscopy (iMIM), a unique optical-pump-electricalprobe technique with 50-nm spatial resolution and 10-ns temporal resolution. Interestingly, the photoconductivity is in general higher in the more defective regions and samples due to the presence of traps that inhibit recombination. Such counterintuitive observations are reconciled by our simultaneous spatial and temporal studies of the photocarrier dynamics in both chemically grown and mechanically exfoliated monolayers. Our results provide fundamental knowledge on the spatiotemporal evolution of charge

Significance

Defects in two-dimensional (2D) transition-metal dichalcogenides play a crucial role in controlling the spatiotemporal dynamics of photogenerated charge carriers, which remain poorly understood to date. In this paper, the defect-mediated carrier diffusion and recombination in WS₂ monolayers are quantitatively investigated by laser-illuminated microwave impedance microscopy. Surprisingly, the photoresponse is in general stronger in the more disordered regions and samples. Such counterintuitive observations are reconciled by spatiotemporally resolved experiments, which indicate that the electron lifetime is prolonged due to the slow release of holes from the trap states. The results reveal the intrinsic time and length scales of photocarriers in van der Waals materials, providing the guidance for implementing nanooptoelectronic devices based on 2D semiconductors.

Author contributions: Z.C. and K.L. designed research; Z.C., C.-Y.W., J.Q., C.Z., C.L., A.H., X.M., H.-L.T., D.A., M.S., X.Z., A.H.M., V.T., X.L., and C.-K.S. performed research; Z.C. and K.L. analyzed data; and Z.C. and K.L. wrote the paper.

The authors declare no competing interest

This article is a PNAS Direct Submission. T.D.K. is a guest editor invited by the Editorial Board.

Published under the PNAS license.

¹Z.C., C.-Y.W., and J.Q. contributed equally to this work.

²To whom correspondence may be addressed. Email: kejilai@physics.utexas.edu.

This article contains supporting information online at https://www.pnas.org/lookup/suppl/doi:10.1073/pnas.2004106117/-/DCSupplemental.

First published June 8, 2020.

carriers in two-dimensional (2D) TMDs, paving the way for their applications in optoelectronic devices.

Experimental Results

We begin our investigation on a chemical-vapor deposited (CVD) WS₂ monolayer (Methods), hereafter denoted as sample A, which presumably has a high level of structural defects (24, 25). The sample is coated by 30-nm atomic-layer deposited (ALD) Al₂O₃ to avoid direct tip-sample contact. Conventional characterization data of the monolayer using atomic-force microscopy (AFM), micro-Raman, and photoluminescence (PL) mapping are included in SI Appendix, Fig. S1. Microwave imaging is carried out using the configuration in Fig. 1A, where the sample is illuminated by a fiber-coupled green laser ($h\nu = 2.4 \text{ eV}$) through the double-side-polished sapphire substrate. The microwave signal at the frequency $f \sim 1$ GHz is delivered to a sharp tip. The real and imaginary parts of the tip-sample admittance are detected by the electronics to form iMIM-Re and iMIM-Im images, respectively (26). Unlike the previous work where the tip was aligned with the laser spot during the sample scan (27-29), there are two sets of piezostages in the current configuration, one moving the focused laser beam to the desired location and the other carrying the tip to scan over the sample and image the diffusion of photoexcited carriers (Fig. 1B). Fig. 1C shows the optical image of sample A with the laser spot in the middle. The iMIM images with and without illumination are displayed in Fig. 1D. The line profiles across the optical

image on a charge-coupled device (CCD) camera and iMIM images at $P_{\rm c}=1.6\times10^6$ mW/cm² are plotted in Fig. 1E, where $P_{\rm c}$ is the laser intensity at the center of the illuminated spot. While the laser shows a Gaussian profile e^{-r^2/w^2} with a width of $w\sim1.5~\mu{\rm m}$, the spatial spread of the iMIM signals clearly exceeds the illumination spot due to carrier diffusion. Interestingly, a slight increase of the iMIM signals is observed at the sample edge, which will be discussed later.

Since the pertinent dimension in this experiment is much smaller than the free-space electromagnetic wavelength at 1 GHz, the iMIM is essentially a near-field impedance probe and the tip-sample interaction is quasielectrostatic in nature (26–29). Quantitative analysis of the iMIM images can be obtained by finite-element modeling (*SI Appendix*, Fig. S2). The localized iMIM response from the region underneath the tip with a dimension comparable to its diameter (*SI Appendix*, Fig. S3) allows us to convert the signals to the local sheet conductance $\sigma_{\rm 2D}$ shown in Fig. 1F. Under the steady-state condition, the spatial distribution of carrier density n(r) follows the diffusion equation (30, 31).

$$n(r) - L^2 \Delta n(r) = \eta \frac{P_c \tau}{h v} e^{-r^2/w^2},$$
 [1]

where $L = \sqrt{D\tau}$ is the diffusion length, $\Delta = \nabla^2$ the Laplace operator, η the incident photon-to-current conversion efficiency

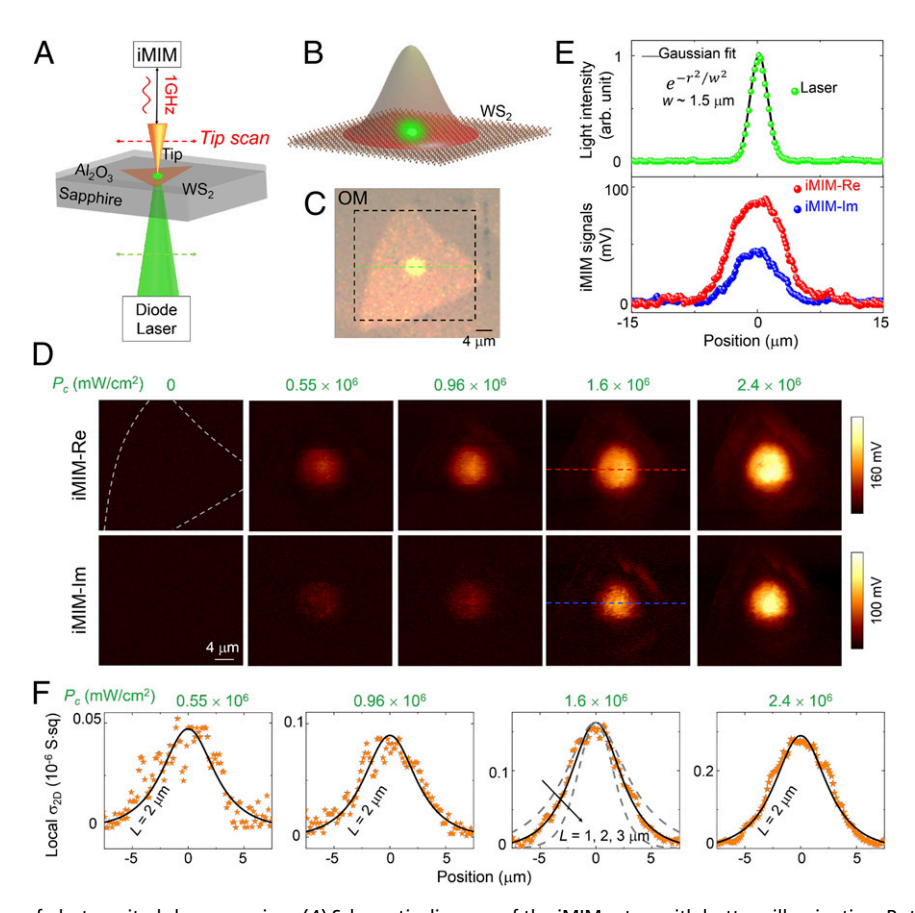


Fig. 1. Diffusion mapping of photoexcited charge carriers. (A) Schematic diagram of the iMIM setup with bottom illumination. Both the tip and the focused laser spot can scan with respect to the sample. The monolayer WS₂ flake grown on double-sided sapphire and coated by ALD Al₂O₃ is also shown in the schematic. (B) Illustration of the carrier diffusion from the illumination spot. (C) Optical reflection image of sample A with the laser spot in the middle. (D) iMIM images inside the dashed box in C at different laser power labeled by the intensity at the center P_c . The dashed lines show the contour of the flake. (E) Line profiles across the CCD (Upper) and iMIM images (Lower) for $P_c = 1.6 \times 10^6$ mW/cm². The solid line is a Gaussian fit to the laser profile with w = 1.5 μm. (F) Measured photoconductivity (orange stars) profiles at various laser intensity. The solid lines show the numerical fits with a diffusion length L = 2 μm. Dashed lines in the panel with $P_c = 1.6 \times 10^6$ mW/cm² correspond to L = 1 and 3 μm.

(IPCE), τ the carrier lifetime, and *D* the diffusion coefficient. The analytical solution to Eq. 1 for a Gaussian laser profile is

$$n(r) \propto \int_{-\infty}^{\infty} K_0(r'/L) e^{-(r-r')^2/w^2} dr',$$
 [2]

where K_0 is the modified Bessel function of the second kind. In the iMIM experiment, the measured 2D sheet conductance can be expressed by

$$\sigma_{\rm 2D} = nq\mu \propto P_c \cdot \tau \cdot \mu, \tag{3}$$

where q is the elemental charge and μ the carrier mobility. It is clear that the photoconductivity scales with the carrier lifetime and mobility, both affected by the presence of defects. Assuming that μ is independent of n within the range of our experiment, we can fit the measured $\sigma_{\rm 2D}$ profiles to Eq. 2. The extracted diffusion length $L=2.0\pm0.3~\mu{\rm m}$ is independent of the laser power, suggesting that bimolecular charge recombination plays a minor role under the steady-state condition here, as is neglected in Eq. 1. We have also confirmed that, as expected, L does not depend on the spot size of the laser beam (SI Appendix, Fig. S4).

To probe the temporal dynamics of photoexcited carriers, we modify the iMIM setup for time-resolved measurements (32). As illustrated in Fig. 24, the laser output is modulated by an electric-optical modulator (EOM), which is driven by a 200-kHz square wave from a function generator. The iMIM signal reaches the steady state within the time of 2.5 μs for each on/off cycle. The low-f filter at the iMIM output stage is also replaced by a high-f amplifier. The microwave signals are synchronized to the EOM and measured by a high-speed oscilloscope. We will only present the iMIM-Im data since the signal is roughly proportional

to σ_{2D} within our measurement range (SI Appendix, Fig. S2). Fig. 2B shows the time-resolved iMIM (tr-iMIM) data averaged over 8,192 cycles at two locations of sample A for $P_c = 2.4 \times$ 10⁶ mW/cm². We note that the steady-state photoconductivity is higher at the edge than that at the center. The apparent rise time $t_{\rm rise} \sim 10$ ns is limited by the temporal resolution of the instrument. On the other hand, the much longer fall time is clearly resolved by our setup. In Fig. 2 C and D (10 times more averaging than that in Fig. 2B), the tr-iMIM signals are plotted in the semilog scale and fitted to biexponential functions $A_1e^{-t/\tau_1} + A_2e^{-t/\tau_2}$. Two relaxation time constants, τ_1 around 100 ns and τ_2 around 1 µs, are observed in both curves. The amplitudes of the two terms are such that $A_1/A_2 \sim 2$ at the center of the WS₂ flake and ~ 0.45 at the edge. Fig. 2E shows the measurement at the same location as Fig. 2C but with a higher optical excitation $P_c = 2.2 \times 10^7 \text{ mW/cm}^2$. A rapid drop of iMIM signal with $t_{\rm drop} \sim 10$ ns, again limited by the temporal resolution, is observed in the beginning of the decay process. It should be noted that finite temporal resolution of iMIM simply means that any processes faster than 10 ns will appear as sudden jumps or rises at that timescale. It does not, however, affect the steady-state signal at t = 0 in Fig. 2 C–E. The multiple timescale indicates that several recombination mechanisms are relevant for photoconductivity in sample A.

The iMIM data of sample A are to be contrasted against those of the mechanically exfoliated flake, hereafter denoted as sample B. In this work, we have carefully isolated WS₂ monolayers from bulk crystals, annealed them under optimal conditions (*Methods*), and protected the surface with \sim 10 nm hexagonal boron nitride (h-BN), as shown in the inset of Fig. 3.4. The much narrower PL spectrum (*SI Appendix*, Fig. S5) of sample B than sample A indicates that the former is cleaner (33), consistent

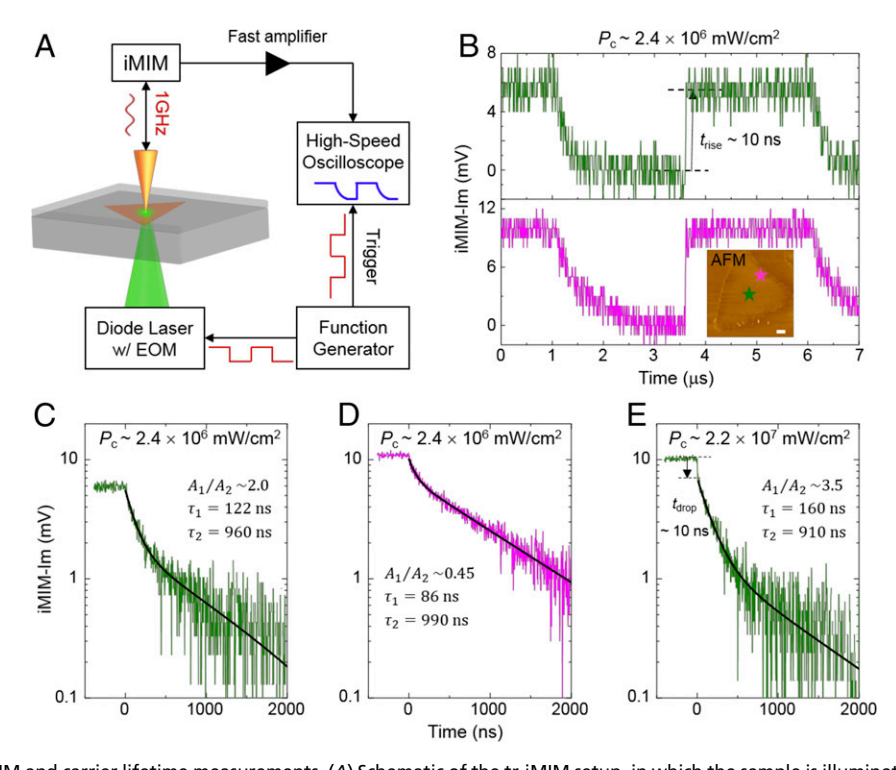


Fig. 2. Time-resolved iMIM and carrier lifetime measurements. (A) Schematic of the tr-iMIM setup, in which the sample is illuminated by a diode laser with its intensity modulated by an EOM. The EOM is driven by a function generator, which also triggers the high-speed oscilloscope that averages the iMIM signals. (B) Time-resolved iMIM-Im signals (averaged over 8,192 cycles) at the center (green) and edge (magenta) of sample A. (Inset) AFM image of the flake, on which the two measured spots are labeled. (Scale bar, 4 μ m.) The rise time of ~10 ns, limited by the temporal resolution of the setup, is indicated in the plot. (C) Relaxation of tr-iMIM signals, averaged over 10 measurements in B, at the center and (D) at the edge of the flake. The solid lines are biexponential fits to the data with two relaxation time constants. (E) Same as C but at a higher laser intensity. A rapid drop of the signal with $t_{\rm drop} \sim 10$ ns, again limited by the temporal resolution, is indicated in the plot.

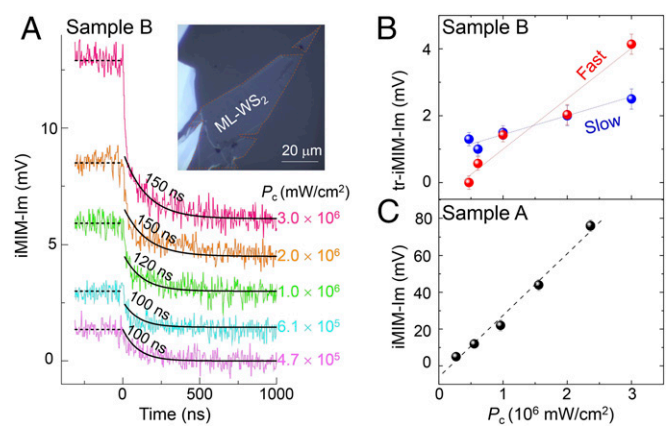


Fig. 3. Time-resolved iMIM results on exfoliated WS₂. (A) Time-resolved data on sample B (optical image in the inset). Except for the lowest laser intensity of 4.7×10^5 mW/cm², the tr-iMIM curves all show a sudden drop faster than our temporal resolution, followed by an exponential decay with time constants of $100 \sim 150$ ns. (B) Amplitudes of the fast (red) and slow (blue) processes in the tr-iMIM data as a function of laser power. The dashed lines are guides to the eyes. (C) Steady-state iMIM-Im signals at the center of the laser spot as a function of P_G taken from Fig. 1D. The dashed line is a linear fit to the data.

with the general view that exfoliated TMD monolayers are usually less defective than the CVD-grown monolayers (34, 35). Surprisingly, during our measurement on over 10 TMD samples, we have systematically observed that the photoconductivity in exfoliated monolayers is always lower than that in CVD ones. Because of the weak iMIM response, a rather blunt tip has to be used to enhance signals in the time-resolved experiments and a high-resolution diffusion mapping is difficult. As seen in Fig. 3A, at the lowest laser intensity $\sim 5 \times 10^5$ mW/cm², the tr-iMIM data show the exponential relaxation with $\tau \sim 100$ ns, which is comparable to τ_1 in sample A. As the laser power increases, however, a resolution-limited rapid process develops in the tr-iMIM signals. As plotted in Fig. 3B, the amplitude of the fast process increases sharply as a function of the laser intensity, whereas the slow process shows a much weaker power dependence. At P_c =

 3×10^6 mW/cm², the fast process has completely dominated the tr-iMIM data. In contrast, for the CVD-grown sample A, the carrier relaxation still follows the slow dynamics up to this power level and the steady-state iMIM-Im signals roughly scale with the laser intensity, as plotted in Fig. 3C.

Discussion

The spatiotemporally resolved iMIM experiments reveal rich and quantitative information of WS₂ monolayers. For sample A, taking the weighted average of $\langle \tau_{center} \rangle \sim 400$ ns and $L \sim 2 \mu m$, we obtain a diffusion coefficient of $D \sim 0.1 \text{ cm}^2/\text{s}$. Using the Einstein relation $D = \mu (k_B T/q)$, where $k_B T$ is the thermal energy, one can show that $\mu \sim 4 \text{ cm}^2/\text{V} \cdot \text{s}$, well within the range of literature values of electron mobility (1 $\sim 10 \text{ cm}^2/\text{V} \cdot \text{s}$) in CVD-grown WS₂ monolayers (36). Based on our transport data (SI Appendix, Fig. S6) and previous iMIM results (27), it is clear that the majority of photoexcited carriers are electrons in the conduction band. Moreover, by substituting the above parameters into Eq. 1, it is straightforward to show that $\eta \sim 0.1\%$ (SI Appendix, Fig. S7), again consistent with previous reports of IPCE in monolayer TMDs (37, 38). Finally, using Eq. 3, where σ_{2D} is obtained from the iMIM data and mobility from the Einstein relation, we can also convert the photoconductivity at various excitation power to the carrier density, as seen in SI Appendix, Fig. S8.

As above-gap photons always excite electron-hole pairs in semiconductors, the predominance of electron transport in photoconduction implies that holes are localized by defects. The presence of structural defects in WS₂ is well documented in the literature (10, 34, 39, 40). Fig. 4A displays scanning transmission electron microscopy (STEM) images of sample A, with three types of defects (S, S-S, W vacancies) clearly resolved. Using first-principles density functional theory (DFT), we can calculate the energy band structures and density of states of these defect configurations. As shown in Fig. 4B, there exist in-gap states that are able to induce Shockley-Read-Hall (41, 42) trap-assisted recombination of mobile carriers. In particular, the midgap states are most effective to annihilate both electrons and holes, whereas the band-tail states are either electron or hole traps, depending on their proximity to the conduction or valence band, respectively. Since as-grown WS2 monolayers are weakly n-doped, it is reasonable to assume that the electron traps are filled. Within

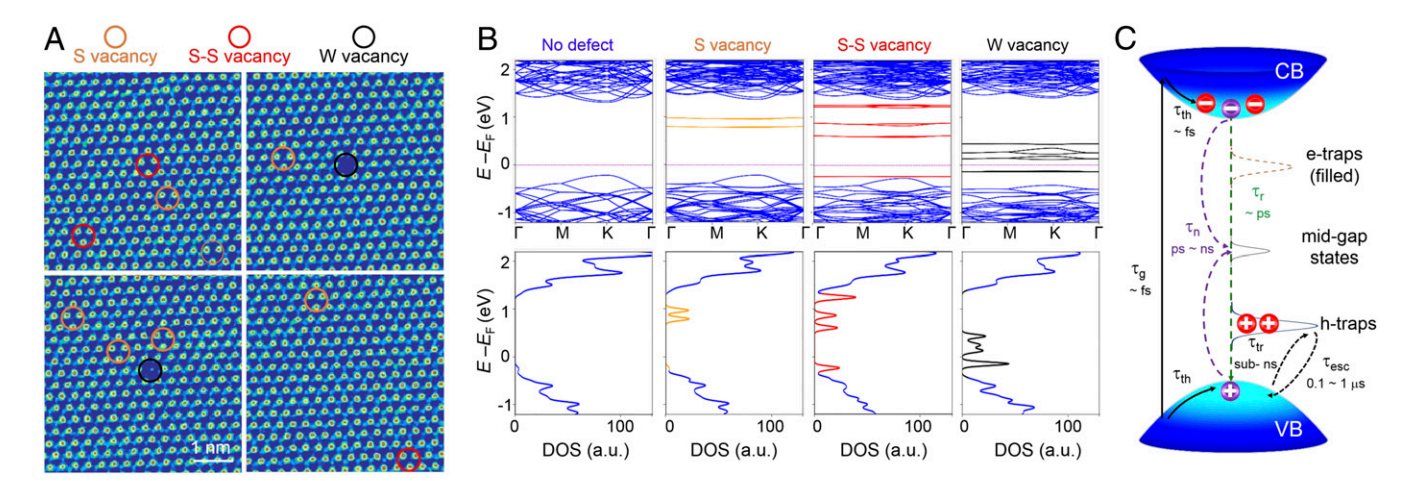


Fig. 4. STEM, DFT, and physical model of the spatiotemporal dynamics. (A) STEM images of the CVD-grown WS₂ sample, showing the presence of atomic defects such as S (orange), S-S (red), and W (black) vacancies. (B) DFT calculations of the energy band structures and density of states for three types of common atomic defects in WS₂ monolayers. (C) Schematic diagram of the band structure with midgap and band-tail states, as well as multiple processes for charge generation and recombination. τ_g , τ_{th} , τ_r , τ_n , τ_{tr} , and τ_{esc} represent the time constant for carrier generation, thermalization, radiative recombination, nonradiative recombination, trapping, and escaping from traps, respectively. Characteristic timescales of these processes are denoted in the plot. Note that the sub-ns exciton lifetime in the radiative recombination process is not relevant for the free-carrier dynamics probes by the iMIM. It is assumed that the electron traps are filled in n-type WS₂ samples, while the hole traps are dominant in the photoconductivity response.

the field of view of our STEM data, five S-S and W vacancies, which lead to trap states near the valence band, are identified. A rough estimate of the defect density is therefore 5×10^{12} cm⁻².

As illustrated in Fig. 4C, the iMIM results allow us to systematically analyze the various processes in the photoresponse of monolayer WS2, which is rather different from traditional semiconductors. Upon photon absorption, electrons and holes are rapidly generated ($\hat{\tau}_g = 10 \sim 100$ fs << 1 ns) and quickly thermalized to the band extrema ($\tau_{th} = 10 \sim 100 \text{ fs} << 1 \text{ ns}$) (43). After that, electron-hole pairs can recombine through various processes. For radiative recombination, mobile electrons and holes only exist for a short time (<1 ps) before forming chargeneutral excitons (not depicted in the schematic). Note that the exciton lifetime $\tau_r = 1 \sim 100$ ps (44–46) is not relevant in this experiment as the typical electric field at the iMIM tip cannot dissociate the tightly bound excitons in monolayer TMDs (SI Appendix, Fig. S2). For nonradiative recombination, midgap states annihilate photogenerated carriers within a lifetime $\tau_n < 1$ ns, as measured by optical and THz pump-probe experiments (47, 48). Band-tail states, on the other hand, trap holes in WS₂ at a fast rate of τ_{tr}^{-1} and slowly release them at a rate of τ_{esc}^{-1} , after which the escaped holes can recombine with electrons within τ_r or τ_n . Since τ_{esc} is much longer than τ_{tr} , the process effectively prolongs the apparent lifetime of electrons in the conduction band (49), which dominates the steady-state photoconductivity at low photon dose. For sample A, the observation of two relaxation time constants ($\tau_1 \sim 100 \text{ ns}, \tau_2 \sim 1 \mu \text{s}$) indicates the presence of a distribution of trap states in the sample. During the CVD growth, it is likely that the outer edge of the flake is more defective than the center, corresponding to a longer average lifetime measured in Fig. 2D. According to Eq. 3, if the dependence of carrier mobility on defect density is relatively modest, the photoconductivity is, counterintuitively, higher in the more defective regions and samples. When the optical excitation increases above a threshold, e.g., $P_c \sim 2 \times 10^7 \text{ mW/cm}^2$ for sample A, the corresponding carrier density of 4×10^{12} cm⁻² is comparable to the defect density estimated from the STEM data. Consequently, trap states are saturated and the excess carriers are annihilated through much faster recombination processes, consistent with the sudden drop in the tr-iMIM data in Fig. 2E. The onset P_c for sample B, however, is only 5×10^5 mW/cm², indicative of much fewer traps in this sample.

As a concluding remark, our findings of the spatiotemporal dynamics in TMDs are important for optoelectronic devices. While ultrafast photoresponse can be detected by pump-probe experiments (44-48), the peak intensity of pulsed laser is usually too high for practical photodetectors. In contrast, the response time of previously demonstrated TMD photodetectors is usually on the order of milliseconds (9, 49–51) or even seconds (22, 52), which is clearly limited by the transport through source/drain contact electrodes. The sub-µs carrier lifetime due to trap states can be inferred from photocurrent measurements (49), which requires device modeling and indirect analysis of the data. In that sense, photoresponse directly probed by the tr-iMIM in the ns-us timescale is not well covered by conventional measurements. A noncontact microwave probe similar to our iMIM setup would take advantage of the sub-µs intrinsic timescale and operate at a much faster speed. Furthermore, while much effort has been made to minimize defects in TMD samples for higher carrier mobility, a moderate amount of defects could actually enhance the photoconductivity, which is favorable for certain device applications.

Conclusion

In summary, we report simultaneous studies of nanoscale spatial distribution and time evolution of photogenerated carriers in WS_2 monolayers by near-field microwave imaging. The diffusion length and carrier lifetime in the CVD-grown sample are

quantitatively measured and analyzed by the diffusion equation. The calculated carrier mobility using the Einstein relation is consistent with the transport result and that in the literature. Time-resolved measurement shows that the $0.1 \sim 1$ -µs dynamics are driven by the slow release of holes from the trap states. Beyond a threshold optical excitation, which is higher in CVD than exfoliated monolayers, the traps are filled and excess carriers are then annihilated by much faster recombination channels. By resolving the spatiotemporal dynamics of carriers, our work represents an important step toward controlling and manipulating carriers in advanced nanooptoelectronic devices based on van der Waals materials.

Methods

Sample Preparation. For the CVD-grown sample on double-side-polished sapphire substrate, solid precursors, including WO $_3$ (300 mg, Sigma-Aldrich Co., 99.995%) and S powders (Sigma-Aldrich Co., 99.5%), were used for the synthesis. The growth of monolayer WS $_2$ was carried out in a 1-in. furnace with a heating rate of 25 °C/min and growth time of 5 min at 1,050 °C. During the growth, the carrying gas of 70 sccm Ar was mixed with 7 sccm of H $_2$, and the gate valve was regulated to keep the pressure at 11.5 mTorr. The S powders were initially heated up to 130 °C for 10 min by a heating tape before the furnace reached the growth temperature. After the growth, the samples were naturally cooled down to ambient temperature under the same H $_2$ /Ar flow.

The exfoliated WS₂ sample was prepared by a dry viscoelastic stamping method. Both h-BN and monolayer WS₂ flakes (bulk crystal from 2Dsemi-conductors Inc.) were mechanically exfoliated from bulk crystals onto a polydimethylsiloxane sheet. Prior to the transfer, we thoroughly cleaned the sapphire substrates with acetone and isopropyl alcohol (IPA) in an ultrasonic bath and subsequent annealing at 800 °C for 10 h. The bottom WS₂ monolayer was first transferred onto the sapphire substrate. The $\sim\!10$ nm h-BN was then transferred on top of the WS₂ monolayer. After each transfer process, the sample was annealed under ultrahigh vacuum (around 10^{-5} mbar) at 300 °C for 6 h.

iMIM and tr-iMIM Setup. The microwave imaging experiment was performed in a customized chamber (ST-500, Janis Research Co.) with positioners and scanners (AttoCube Systems AG). The Ptlr probe tip (12Ptlr400A, Rocky Mountain Nanotechnology LLC) was mounted on the xyz scanner for tip scans. For the diffusion mapping experiment, the CW laser intensity was modulated by an optical chopper with a frequency of 1 kHz to improve the signal-to-noise ratio. For the tr-iMIM experiment, the low-f amplifier (54 dB, 20 kHz) after the microwave mixer was replaced by a fast amplifier (28 dB, 350 MHz, SR445A, Stanford Research Systems Inc.). The diode laser was modulated by an electric-optical modulator (M350-160-01 EOM, Conoptics Inc.) with a power supply of 8-ns rise/fall time. The EOM was driven by a 200-kHz square wave from a function generator (DG5071, RIGOL Technologies USA Inc.) with <4-ns rise/fall time. The tr-iMIM signals were measured by a 600-MHz oscilloscope (DS6062, RIGOL Technologies USA Inc.) with 5-GSa/s sampling rate. The time resolution of our setup is about 10 ns.

STEM Preparation and Characterization. The WS₂ monolayers were coated by polymethylmethacrylate (PMMA) polymer and the PMMA/WS₂/sapphire sample was annealed at 120 °C in air for 10 min. The sample was then put into the diluted hydrogen fluoride (HF) solution for 5 min to separate the PMMA/WS₂ film from the sapphire surface. The 400-mesh nickel TEM grid was used to pick up the film. The PMMA was then removed by acetone for more than 1 h. The TEM grid with WS₂ crystals was finally baked in vacuum (<10⁻⁶ Torr) at 350 °C for overnight to remove the PMMA residue. The STEM measurement was conducted at 80 kV using a ThermoFisher USA (former FEI Co.) Titan Themis Z (40–300 kV) TEM equipped with a double-Cs (spherical aberration) corrector, a high-brightness electron gun (x-FEG), and Fischione STEM detector.

First-Principles DFT Calculations. DFT calculations were performed using the Vienna *Ab initio* Simulation Package (VASP), in which Generalized gradient approximations of Perdew–Burke–Ernzerhof have been adopted for exchange-correlation potential. In the model, a supercell is composed of 5×5 WS₂ unit cells and a 20-Å-thick vacuum. The lattice constant of a unit cell is 3.19 Å. For the calculation of energy band structures and density of states, 5×5 supercells were used. Four types of calculations were performed: pristine monolayer WS₂ and three types of defects (W, S, or S-S) with defects density 10^{13} cm⁻². During

the self-consistent (SC) calculations, the global break condition for the electronic SC loop is set to be 10^{-7} eV, the cutoff energy for the plane-wave basis set is 400 eV, and k-point sampling is $8\times8\times1$ with a Gaussian smearing method, in which the smearing width is 0.05 eV.

Data Availability. All data supporting the findings of this study are present in the manuscript and/or *SI Appendix*.

ACKNOWLEDGMENTS. The research at The University of Texas at Austin (UT-Austin), performed collaboratively between K.L., C.-K.S., X.L., and A.H.M., was primarily supported by the NSF through the Center for Dynamics and Control of Materials, an NSF Materials Research Science and Engineering Center (MRSEC) under Cooperative Agreement DMR-1720595. The authors also acknowledge the use of facilities and instrumentation supported by the NSF MRSEC. K.L., C.-K.S., and X.L. were also supported by NSF Award EFMA-

- 1. K. F. Mak, C. Lee, J. Hone, J. Shan, T. F. Heinz, Atomically thin MoS₂: A new direct-gap semiconductor. *Phys. Rev. Lett.* **105**, 136805 (2010).
- K. F. Mak, K. He, J. Shan, T. F. Heinz, Control of valley polarization in monolayer MoS2 by optical helicity. Nat. Nanotechnol. 7, 494–498 (2012).
- 3. A. M. Jones et al., Optical generation of excitonic valley coherence in monolayer WSe₂. Nat. Nanotechnol. **8**, 634–638 (2013).
- 4. F. Xia, H. Wang, M. D. Di Xiao, A. Ramasubramaniam, Two-dimensional material nanophotonics. *Nat. Photonics* **8**, 899–907 (2014).
- K. F. Mak, J. Shan, Photonics and optoelectronics of 2D semiconductor transition metal dichalcogenides. Nat. Photonics 10, 216–226 (2016).
- L. Britnell et al., Strong light-matter interactions in heterostructures of atomically thin films. Science 340, 1311–1314 (2013).
- A. Allain, A. Kis, Electron and hole mobilities in single-layer WSe₂. ACS Nano 8, 7180–7185 (2014).
- A. Splendiani et al., Emerging photoluminescence in monolayer MoS₂. Nano Lett. 10, 1271–1275 (2010).
- D.-S. Tsai et al., Few-Layer MoS2 with high broadband Photogain and fast optical switching for use in harsh environments. ACS Nano 7, 3905–3911 (2013).
- Z. Lin et al., Defect engineering of two-dimensional transition metal dichalcogenides. 2D Mater. 3, 22002 (2016).
- H. Liu et al., Statistical study of deep submicron dual-gated field-effect transistors on monolayer chemical vapor deposition molybdenum disulfide films. Nano Lett. 13, 2640–2646 (2013).
- T. H. Ly et al., Misorientation-angle-dependent electrical transport across molybdenum disulfide grain boundaries. Nat. Commun. 7, 10426 (2016).
- A. Srivastava et al., Optically active quantum dots in monolayer WSe2. Nat. Nanotechnol. 10. 491–496 (2015).
- M. Koperski et al., Single photon emitters in exfoliated WSe2 structures. Nat. Nanotechnol. 10, 503–506 (2015).
- Y.-M. He et al., Single quantum emitters in monolayer semiconductors. Nat. Nanotechnol. 10, 497–502 (2015).
- C. Chakraborty, L. Kinnischtzke, K. M. Goodfellow, R. Beams, A. N. Vamivakas, Voltage-controlled quantum light from an atomically thin semiconductor. *Nat. Nanotechnol.* 10, 507–511 (2015).
- S. Kim et al., Interstitial Mo-Assisted photovoltaic effect in multilayer MoSe2 phototransistors. Adv. Mater. 30, e1705542 (2018).
- H. R. Gutiérrez et al., Extraordinary room-temperature photoluminescence in triangular WS₂ monolayers. Nano Lett. 13, 3447–3454 (2013).
- G. Moody et al., Microsecond valley lifetime of defect-bound excitons in monolayer WSe_2. Phys. Rev. Lett. 121, 57403 (2018).
- D. V. Lang, C. H. Henry, Scanning photocurrent microscopy: A new technique to study inhomogeneously distributed recombination centers in semiconductors. Solid-State Electron. 21, 1519–1524 (1978).
- C.-C. Wu et al., Elucidating the photoresponse of ultrathin MoS₂ field-effect transistors by scanning photocurrent microscopy. J. Phys. Chem. Lett. 4, 2508–2513 (2013).
- O. Lopez-Sanchez, D. Lembke, M. Kayci, A. Radenovic, A. Kis, Ultrasensitive photodetectors based on monolayer MoS2. Nat. Nanotechnol. 8, 497–501 (2013).
- B. W. H. Baugher, H. O. H. Churchill, Y. Yang, P. Jarillo-Herrero, Optoelectronic devices based on electrically tunable p-n diodes in a monolayer dichalcogenide. *Nat. Nanotechnol.* 9, 262–267 (2014).
- 24. Z. Liu et al., Identification of active atomic defects in a monolayered tungsten disulphide nanoribbon. Nat. Commun. 2, 213 (2011).
- J. Hong et al., Exploring atomic defects in molybdenum disulphide monolayers. Nat. Commun. 6, 6293 (2015).
- K. Lai, W. Kundhikanjana, M. Kelly, Z. X. Shen, Modeling and characterization of a cantilever-based near-field scanning microwave impedance microscope. Rev. Sci. Instrum. 79, 63703 (2008).

1542747. The iMIM instrumentation was supported by the US Army Research Laboratory and the US Army Research Office under Grants W911NF-16-1-0276 and W911NF-17-1-0190. K.L. and Z.C. acknowledge the support from Welch Foundation Grant F-1814. X.L. acknowledges the support from Welch Foundation Grant F-1662. J.Q. acknowledges the support from the Department of Energy, Basic Energy Science Grant DE-SC0019398 and a catalysis grant from the UT-Austin. C.Z. and X.Z. acknowledge the financial support from King Abdullah University of Science and Technology, Office of Sponsored Research under Award CRF-2016-2996-CRG5. V.T. gratefully acknowledges the research award from the Doctoral New Investigator Award from American Chemical Society (ACS) Petroleum Fund (Award ACS) PRF 54717-DNI10). Part of the characterization and synthesis of 2D TMDs in this work was performed as User Proposals (5067 and 5424) at the Molecular Foundry, Lawrence Berkeley National Laboratory, supported by the Office of Basic Energy Sciences, of the US Department of Energy under Contract DE-AC02-05CH11231.

- Y. Tsai et al., Tailoring semiconductor lateral multifunctions for giant photoconductivity enhancement. Adv. Mater. 29, 1703680 (2017).
- Z. Chu et al., Impact of grain boundaries on efficiency and stability of organicinorganic trihalide perovskites. Nat. Commun. 8, 2230 (2017).
- Z. Chu et al., Energy-resolved photoconductivity mapping in a monolayer-bilayer WSe₂ lateral heterostructure. Nano Lett. 18, 7200–7206 (2018).
- T. Kato, T. Kaneko, Transport dynamics of neutral excitons and trions in monolayer WS₂, ACS Nano 10, 9687–9694 (2016).
- F. Cadiz et al., Exciton diffusion in WSe₂ monolayers embedded in a van der Waals heterostructure. Appl. Phys. Lett. 112, 152106 (2018).
- S. R. Johnston, E. Y. Ma, Z.-X. Shen, Optically coupled methods for microwave impedance microscopy. Rev. Sci. Instrum. 89, 43703 (2018).
- G. Moody et al., Intrinsic homogeneous linewidth and broadening mechanisms of excitons in monolayer transition metal dichalcogenides. Nat. Commun. 6, 8315 (2015).
- 34. W. Zhou et al., Intrinsic structural defects in monolayer molybdenum disulfide. Nano Lett. 13, 2615–2622 (2013).
- S.-J. An, Y. H. Kim, C. Lee, D. Y. Park, M. S. Jeong, Exfoliation of transition metal dichlcogenides by a high-power femtosecond laser. Sci. Rep. 8, 12957 (2018).
- 36. Z.-Q. Xu et al., Synthesis and transfer of large-area monolayer WS₂ crystals: Moving toward the recyclable use of sapphire substrates. ACS Nano 9, 6178–6187 (2015).
- 37. Y. Gong et al., Two-step growth of two-dimensional WSe2/MoSe2 heterostructures. Nano Lett. 15, 6135–6141 (2015).
- C. Li et al., Engineering graphene and TMDs based van der Waals heterostructures for photovoltaic and photoelectrochemical solar energy conversion. Chem. Soc. Rev. 47, 4981–5037 (2018).
- S. Yuan, R. Roldan, M. I. Katsnelson, F. Guinea, Effect of point defects on the optical and transport properties of MoS2 and WS2. Phys. Rev. B 90, 041402(R) (2014).
- M. R. Rosenberger, H.-J. Chuang, K. M. McCreary, C. H. Li, B. T. Jonker, Electrical characterization of discrete defects and impact of defect density on photoluminescence in monolayer WS₂. ACS Nano 12, 1793–1800 (2018).
- W. Shockley, W. T. Read Jr., Statistics of recombinations of holes and electrons. Phys. Rev. 87, 835 (1952).
- 42. R. N. Hall, Electron-hole recombination in germanium. Phys. Rev. 87, 387 (1952).
- A. Grubišić Čabo et al., Observation of ultrafast free carrier dynamics in single layer MoS₂. Nano Lett. 15, 5883–5887 (2015).
- C. Robert et al., Exciton radiative lifetime in transition metal dichalcogenide monolayers. Phys. Rev. B 93, 205423 (2016).
- L. Yuan, T. Wang, T. Zhu, M. Zhou, L. Huang, Exciton dynamics, transport, and annihilation in atomically thin two-dimensional semiconductors. J. Phys. Chem. Lett. 8, 3371–3379 (2017).
- A.J. Goodman et al, Suppressing diffusion-mediated exciton annihilation in 2D semiconductors using the dielectric environment. arXiv:1811.01066 (2 November 2018)
- 47. R. Wang et al., Ultrafast and spatially resolved studies of charge carriers in atomically thin molybdenum disulfide. *Phys. Rev. B* **86**, 45406 (2012).
- S. Kar, Y. Su, R. R. Nair, A. K. Sood, Probing photoexcited carriers in a few-layer MoS2 laminate by time-resolved optical pump-terahertz probe spectroscopy. ACS Nano 9, 12004–12010 (2015)
- M. M. Furchi, D. K. Polyushkin, A. Pospischil, T. Mueller, Mechanisms of photoconductivity in atomically thin MoS₂. Nano Lett. 14, 6165–6170 (2014).
- N. Perea-Lopez et al., Photosensor device based on few-layered WS₂ films. Adv. Funct. Mater. 23, 5511–5517 (2013).
- 51. Z. Yang et al., Spatial/temporal photocurrent and electronic transport in monolayer molybdenum disulfide grown by chemical vapor deposition. *Appl. Phys. Lett.* **108**, 92104 (2016)
- 52. W. Zhang et al., High-gain phototransistors based on a CVD MoS₂ monolayer. Adv. Mater. 25, 3456–3461 (2013).